Modeling, Control, and Performance Evaluation of Grid-Tied Hybrid PV/Wind Power Generation System: Case Study of Gabel El-Zeit Region, Egypt

AHMAD F. TAZAY[ID]1, AHMED MOHAMMED AHMED IBRAHIM2, OMAR NOURELDEEN1,2, AND I. HAMDAN2

[1]Electrical Engineering Department, Faculty of Engineering, Baha University, Al Bahah 65527, Saudi Arabia
[2]Electrical Engineering Department, Faculty of Engineering, South Valley University, Qena 83523, Egypt

Corresponding author: Ahmad F. Tazay (afareed@bu.edu.sa)

ABSTRACT The potential for utilizing clean energy technologies in Egypt is excellent given the abundant solar irradiation and wind resources. This paper provides detailed design, control strategy, and performance evaluation of a grid-connected large-scale PV/wind hybrid power system in Gabel El-Zeit region located along the coast of the Red Sea, Egypt. The proposed hybrid power system consists of 50 MW PV station and 200 MW wind farm and interconnected with the electrical grid through the main Point of Common Coupling (PCC) busbar to enhance the system performance. The hybrid power system is controlled to operate at the unity power factor and also the Maximum Power Point Tracking (MPPT) technique is applied to extract the maximum power during the climatic conditions changes. Modeling and simulation of the hybrid power system have been performed using MATLAB/SIMULINK environment. Moreover, the paper presented a comprehensive case study about the realistic monthly variations of solar irradiance and wind speed in the study region to validate the effectiveness of the proposed MPPT techniques and the used control strategy. The simulation results illustrate that the total annual electricity generation from the hybrid power system is 1509.85 GWh/year, where 118.15 GWh/year (7.83 %) generates from the PV station and 1391.7 GWh/year (92.17%) comes from the wind farm. Furthermore, the hybrid power system successfully operates at the unity power factor since the injected reactive power is kept at zero.

INDEX TERMS PV, wind, hybrid system, Gamesa G80, Gabel El-Zeit, Egypt.

LIST OF ABBREVIATIONS

RES	Renewable Energy Sources
NREA	New and Renewable Energy Authority
PCC	Point of Common Coupling
MPPT	Maximum Power Point Tracking
InCond	Incremental Conductance
VSI	Voltage Source Inverter
GSC	Grid Side Converter
WECS	Wind Energy Conversion System
RSC	Rotor Side Converter
MPP	Maximum Power Point
VOC	Voltage-Oriented Control
PLL	Phase-Locked Loop
DFIG	Doubly Fed Induction Generator
SFOC	Stator Flux-Oriented Control
P&O	Perturb and Observe

LIST OF SYMBOLS

V_{10}, V_h	Average wind speed at a hub height of 10 m and 60 m
h, α	Hub height above sea level and the roughness factor
V, I	Terminal voltage and output current of the PV module
P	The output power of the PV module
N	Scaling factor which adjusts the duty cycle size
d, q	subscribe d-q axis components in the synchronously rotating reference frame
s, r	Subscribe stator and rotor windings
V, i, ϕ	Denote voltage, current and flux linkage
V_{d-inv}, V_{q-inv}	d-q axis components of the VSI voltage
V_d, V_q	d-q axis components of the PCC bus voltage
ω_e	Rotation speed of the d-q synchronous reference frame

I_d, I_q	d-q axis components of the VSI current
R_f, L_f	Resistance and inductance of the PV station filter
K_p, K_i	Proportional and integral gains of PI controller
R, L	Resistance and self-inductance of the DFIG
L_m	Magnetizing inductance of the DFIG
I_{dr-ref}, I_{qr-ref}	Reference d-q axis components of the rotor current
V_{dr-ref}, V_{qr-ref}	Reference d-q axis components of the rotor voltage
I_{dg-ref}, I_{qg-ref}	Reference d-q axis components of the GSC current
σ_s, i_{ms}	Stator leakage factor and stator magnetizing current
ω_r, ω_{ref}	Actual and optimum rotational speed of DFIG rotor
V_{dc2}, C_2	DC-bus voltage and capacitance of DC-bus capacitor
W	Energy stored in the DC-link capacitor
m, i_{or}	Stator modulation factor and the DC-Bus current
L_{choke}	The inductance of the DFIG filter
M	Scaling factor that adjusts step-size of change in rotor speed

I. INTRODUCTION

Nowadays, the combined utilization of Renewable Energy Sources (RES) such as PV and wind energy is being widely used for substitution of conventional energy resources, and eventually to decrease the combustion of fossil fuels. Moreover, in terms of its environmental advantages, the RES generate electricity without emission of greenhouse gases or carbon dioxide (CO_2) to the atmosphere and they also produce no pollution on soil or water. In Egypt, the potential of using clean energy technologies is excellent given the abundant wind resources and solar irradiation. Egypt is endowed with large solar energy resources since it is one of the sun-belt area countries, where the solar Atlas of Egypt indicates that the duration of daily sunshine ranges between 9-11 hours/day. Also, the mean annually solar radiation is between 2000-3200 kWh/m^2/year, which enhances great opportunities for development in the solar energy fields in Egypt [1], [2]. Historically, the first Egyptian thermal solar power plant with a total installed capacity of 140 MW has been built in Kuraymat in 2011, of which, 20 MW was the solar power share. Then, in the Siwa Oasis in Western Sahara, a solar power station with a rated power of 10 MW has been installed since March 2015. Also, in April 2016, four PV plants were operated 14 MW in Egypt's Red Sea Governorate to support the area's vital tourism sector. Currently, Egypt will plan to possess solar energy with a total capacity of 3.5 GW by 2027; including 2.8 GW from the PV energy and 0.7 GW from the Concentrated Solar Power (CSP). Recently, the New and Renewable Energy Authority (NREA) in Egypt has embarked

on an ambitious project to build the biggest PV power station worldwide, with a total generation capacity of 1.8 GW. The project includes installation and operation of 41 individual PV power plants that spread across 37.2 Km^2 in the south of the Egyptian territory in Benban, Aswan [3].

On the other hand, wind energy in Egypt is regarded as one of the most promising renewable energy sources and it has continued to be the fastest-growing in terms of the generated power because of its economic viability. Historically, the first Egyptian wind farm consisting of 700 wind turbines with a total power capacity of 545 MW has been established in Zafarana in several stages since 2001. Moreover, Gabel El-Zeit region located along the coast of the Red Sea is very rich with great wind energy resources that could reach about 20,000 MW, where the average wind speed is approximately 9 m/s at 10 m height [4], [5]. Therefore, two large-scale wind farms projects have been implemented in Gabel El-Zeit region. The first project is Gabel El-Zeit 1 wind farm was consisting of 120 wind turbines with a total power capacity of 240 MW that was built in 2010. Then, the second project is Gabel El-Zeit 2 wind farm consisting of 110 wind turbines with a total power capacity of 220 MW that has been completed since July 2018. Furthermore, the annual growth of the wind power generation in Egypt has developed exponentially during the period from 2010 to 2017, as shown in Fig. 1. Recently, the strategy of the NREA in Egypt aims to supply 12% of the total electricity generation from the wind energy by the end of 2020, which means increasing the installed wind power capacity to 7200 MW [3], [6].
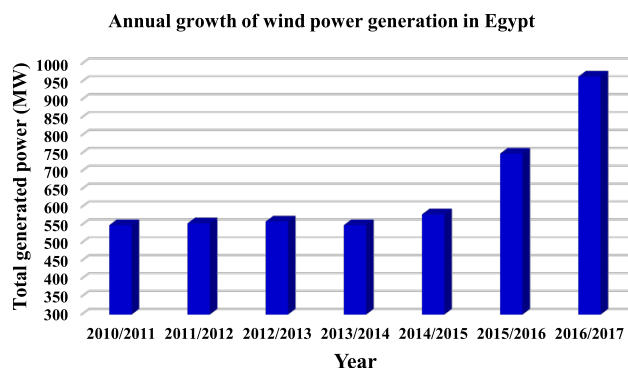

FIGURE 1. Annual growth of wind power generation in Egypt [3].

Over recent years, many studies in the field of using the RES in Egypt have been reported. Among them, a comprehensive study for selecting the optimum locations to implement large-scale grid-connected PV power stations in Egypt has been discussed in [2], [4]. The study analyzed the availability of vacant areas for installation, environmental conditions, economics profits, and the future developments related to the implementation of the PV stations in the selected sites. Moreover, in terms of using wind energy in Egypt, Noureldeen *et al.* [6], proposed an advanced artificial intelligence protection technique based on Low Voltage Ride-Through (LVRT) for a large-scale grid-connected wind farm.

The proposed protection technique is applied to a simulation model of 200 MW Gabel El-Zeit wind farm as a case study in Egypt. Hatata and Rana Elmahdy [5], assessed the wind energy potentiality in different sites in Egypt. The paper recommended that Gabel El-Zeit region is the most feasible location in Egypt to build large-scale wind plants, where the average wind speed reaches about 9 m/s at a height of 10 m. In [7], the paper investigated the impact of extreme gust occurrence on the Gulf El-Zayt wind farm. The obtained results illustrate the influence of various extreme gust wind speed fluctuations on the variation of the generated active power and reactive power from the wind farm. Also, Noureldeen *et al.* [8], utilized the STATCOM and the supercapacitor to provide stability improvement of 200 MW Gabel El-Zeit wind farm during a severe wind gust occurrence as a case study of the wind speed variation.

In [9], the paper presented a detailed feasibility study using HOMER software about applying a hybrid system consisting of PV, wind, diesel generator, and battery to supply the electrical energy needs for an environmentally-friendly city (New Borg El Arab) in Egypt. Also, a reliable optimization methodology incorporated Mine Blast Algorithm (MBA) has been applied in [10] to determine the optimal size of a PV/wind/fuel cell hybrid system supplying the electrical power to a rural area in Egypt. However, to the best of found knowledge, most previous researches have been confined in the optimization studies to determine the optimal location or the optimal size of a single renewable energy source. No large-scale attempts have been made to implement the hybrid renewable energy systems in Egypt, where more than one power generation source is applied. Additionally, few researchers have focused on the integration of large-scale hybrid renewable power systems with the electrical grid.

From the literature survey and to utilize the RES in Egypt, this paper presents the detailed design, control strategy, and performance analysis of a grid-connected large-scale PV/wind hybrid power system in Gabel El-Zeit region located along the coast of the Red Sea, Egypt. This region is endowed with a good level of solar irradiance with an annual average value of 199.75 kWh/m2 and powerful wind speed with an average value of 14.08 m/s at 60 m hub height. The proposed hybrid power system consists of 50 MW PV station-based Sanyo HIP-200B PV module and 200 MW wind farm-based Gamesa G80 wind turbine and it is interconnected with the electrical grid through the main PCC busbar to enhance the system performance. An adaptive variable step-size MPPT algorithm is applied to extract the maximum power from the PV station, while a modified P&O MPPT strategy is implemented to capture the peak power from the wind farm. Also, the hybrid power system is controlled to operate at the unity power factor during all the environmental conditions. The dynamic performance of the hybrid power system is evaluated during realistic changes in solar irradiance and wind speed in the study region to validate the efficiency of the MPPT techniques and the applied control strategy.

II. THE LONG-TERM CLIMATIC CONDITIONS IN THE SITE UNDER STUDY

Climatic conditions including solar radiation and wind speed are the main factors that determine the availability of the PV and wind energy at any site. The site under study is Gabel El-Zeit region situated in the North-Eastern Desert, on the western coast of the Suez Gulf, Egypt, as shown in Fig. 2. It is located between longitudes 33° 30' and 24° 55' E, and latitudes 27° 56' and 28° 10' N [11], [12]. The potential for utilizing clean energy technologies in Gabel El-Zeit is excellent given the abundant solar irradiation and wind resources. The study area has of solar irradiance which ranges from 172.1 W/m^2 in December to 353.4 W/m^2 in July with an annual average value of 273.42 W/m^2, as shown in Fig. 3 and Table 1. Irradiance data is gathered from the solar Atlas of Egypt [13].

FIGURE 2. Location map of Gabel El-Zeit area (site under study) [12].
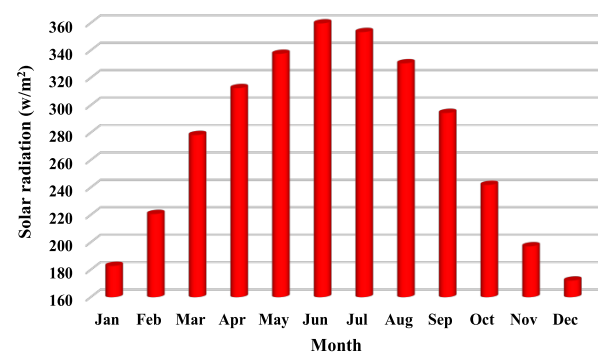

FIGURE 3. The average monthly solar radiation data [13].

Moreover, Gabel El-Zeit is characterized by powerful wind speed which ranges between 12.44 m/s in November and

TABLE 1. The average monthly solar irradiation and wind speed in Gabel El-Zeit region.

Month	Jan	Feb	Mar	Apr	May	Jun	Jul	Aug	Sep	Oct	Nov	Dec	Annual average
Solar Radiation (w/m2)	182.8	220.7	278.3	312.5	337.5	359.7	353.4	330.6	294.4	241.9	197.1	172	273.42
wind speed at 60 m (m/s)	13.18	13.18	14.57	14.85	14.92	15.62	14.54	14.34	14.51	14.07	12.44	12.71	14.08
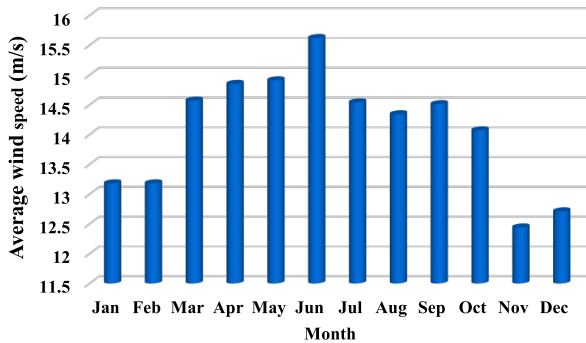
FIGURE 4. The average monthly wind speed data at 60 m height [5].

FIGURE 5. Configuration of the proposed PV/wind hybrid system.

15.62 m/s in June with an annual average value of 14.08 m/s, as shown in Fig. 4 and Table 1. The wind speed profile is obtained from the wind speed data at the standard 10 m height which gathered from the Egyptian Meteorological Authority based on measurements for more than 10 years [5]. The variation of wind speed can be expressed as follows [5], [7]:

$$V_h = V_{h_r}(\frac{h}{h_r})^\alpha \qquad (1)$$

where α is the power-law index or the roughness factor which is selected to be 0.25 to represent the most appropriate value for the terrain and the wind conditions in Egypt [5], [7]. V_h is the average wind speed at wind turbine's hub height (m/s), h_r is the height of wind speed measurement which equals 10 (m), h is the height of the wind turbine's hub location, (m).

III. SYSTEM CONFIGURATION

The configuration of the proposed PV/wind hybrid generation system is shown in Fig. 5 and its detailed specifications are summarized in Table 2. It consists of 50 MW PV station and 200 MW wind farm are interconnected with the electrical network through the main PCC busbar to enhance the system performance. In this study, 5 PV modules are connected in series, and a total of 50,000 branches are parallel-connected to achieve the rated power of the PV station (50 MW). Sanyo HIP-200B PV module with a peak power of 200.3 W is utilized for this work [14]. An adaptive InCond MPPT technique is implemented on the boost converter to extract the maximum power from the PV station during the change of solar irradiance. Also, a 3-level, 3-phase Voltage Source Inverter (VSI) is used for interfacing the PV station with the electrical grid.
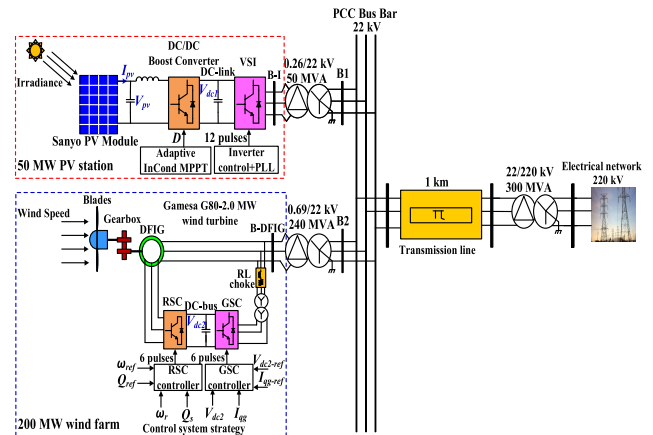
The wind farm with a rated power of 200 MW consists of 100 variable-speed Doubly Fed Induction Generator (DFIG)-based wind turbines from Gamesa G80-2.0 MW type. The DFIG stator winding is connected to the PCC bus through a 0.69/22 kV step-up transformer, while the rotor winding is connected to the low voltage side of the step-up transformer by a back-to-back converter and a transformer. The back-to-back converter consists of two converters Grid Side Converter (GSC) and Rotor Side Converter (RSC) coupled by a DC-bus capacitor. The GSC is used to sustain the DC-bus voltage constant and regulate the exchanged reactive power between the back-to-back converter and the grid. Also, a modified P&O MPPT strategy is applied to the RSC to capture the peak power from the wind farm during the wind speed variation. Moreover, the hybrid power system is adjusted to operate at unity power factor and the generated power is injected into the electrical grid through 1 km double circuit transmission lines and 22/220 kV Δ/Y step-up transformer.

A. PV STATION CONFIGURATION

1) SELECTION OF THE PV MODULE

The PV plant with a rated power of 50 MW contains 500 PV arrays electrically connected in parallel, each array consists of 100 parallel-connected strings that formed by connecting 5 PV modules in series. To determine the most appropriate PV module to be used in this work, a large-scale survey about the PV modules characteristics from different manufacturers is needed. El-Shimy [4], presented a comprehensive survey about the characteristics of most of the available PV panels

TABLE 2. Design specification of the proposed PV/wind hybrid power system.

| PV station parameters		Wind farm parameters	
Rated power	50 MW	Rated power of wind farm	200 MW
PV module type	Sanyo HIP-200BA20	Wind turbine type	Gamesa G80
Rated power of the PV module	200.3 W	Rated power of wind turbine	2 MW
Number of parallel arrays	500	Cut-in wind speed	3.5 m/s
Number of parallel strings per array	100	Rated wind speed	15 m/s
Number of series modules per string	5	Cut-out wind speed	25 m/s
Nominal DC-link voltage	500 V	Survival wind speed	55.8 m/s
Power factor of DC/AC Inverter	Unity	Rotor diameter	80 m
Transmission lines parameters		Swept area by turbine blades	5027 m2
Length of transmission line	1 Km	Number of rotor blades	3
Positive sequence resistance	0.1153 Ω /Km	Max rotor speed	1900 rev/min
Zero sequence resistance	0.413 Ω /Km	Tip speed	80 m/s
Positive sequence inductance	1.05 mH/Km	Power density	397.9 w/m2
Zero sequence inductance	3.3 mH/Km	Gearbox stages	3
Positive sequence capacitance	11.33 nF/Km	Gearbox ratio	1:101
Zero sequence capacitance	5.01 nF/Km	Generator type	DFIG
Grid parameters		Stator voltage	690 V
Grid voltage	220 kV	Grid frequency	50 Hz
Grid frequency	50 Hz	Nominal DC-bus voltage	1150 V
S.C level	1000 MVA	Stator resistance of DFIG	0.023 p.u
X/R	8	Rotor resistance of DFIG	0.016 p.u
		Optimal tip speed ratio (λopt)	8.1
		Optimal performance coefficient (Cp-opt)	0.48
		Hub height	60 m
		Tower-type	steel tube
		Tower shape	Conical

in the market whose efficiency greater than 15% and formed a list of the candidate modules. Based on the survey and the selection criteria of the maximum module capacity/area, Sanyo HIP-200B PV module with a maximum power of 200.3 W is selected in this study. Table 3 summarizes the specification of the Sanyo PV module and the rest of the detailed specifications are available in [14]. The modeling of the PV module is implemented using the equations described in [15]. Also, the current-voltage (I-V) and the power-voltage (P-V) characteristics of the selected PV module during the change of the solar irradiation are shown in Fig. 6.

**TABLE 3.** The detailed specification of the Sanyo PV module.

Model	Sanyo HIP-200BA20
Rated power	200.3 W
Open circuit Voltage of PV module	68.7 V
Short-circuit current of PV module	3.83 A
Voltage at the MPP	55.8 V
Current at the MPP	3.59 A
Number of cells in series	96
Module efficiency	17 %
Cell efficiency	19.7 %
Temperature coefficient of Voc	-0.77%/ ºC
Dimensions	1,319*894*35 mm
Module area	1.18 m^2
Weight	14 kg
Standard Operating Conditions (SOC) T= 25 ˚C, G=1000 W/m^2	

2) BOOST CONVERTER CONTROLLER: ADAPTIVE VARIABLE STEP-SIZE INCOND MPPT TECHNIQUE

The PV station is also controlled so that it operates at its Maximum Power Point (MPP). In this work, an adaptive InCond MPPT strategy is utilized to extract the maximum
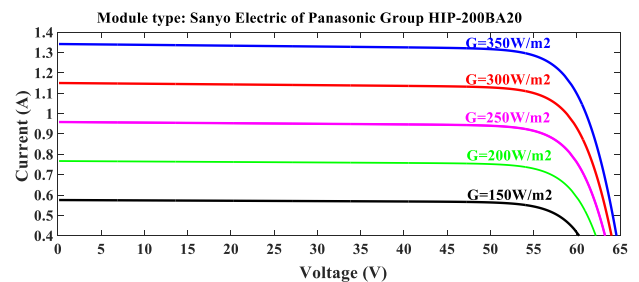
(a) Current-voltage (I-V) characteristics
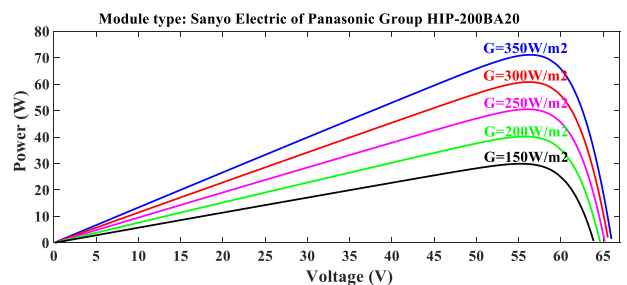
(b) Power-voltage (P-V) characteristics

FIGURE 6. Characteristics of the Sanyo PV module.

power from the PV station and enhance its overall efficiency during the change of solar irradiance. This strategy provides efficient tracking of the MPP and avoids the drift problem during the rapid variation of the solar irradiance. The drift problem occurs due to the lack of knowledge in determining whether the increase in power is due to the perturbation of the PV module output voltage or due to the irradiance increase. Practical ways of addressing this issue in real situations have

been studied extensively in [16]. The proposed MPPT algorithm depends on the fact that the change of power concerning voltage (dP/dV) is equal to zero at the MPP, negative at the right of MPP, and positive at the left of MPP. This MPPT method can be expressed mathematically as [17]–[19]:

$$P = IV \tag{2}$$

$$\frac{dP}{dV} = \frac{d}{dV}[IV] = V\frac{dI}{dV} + I \tag{3}$$

$$\frac{dP}{dV} = 0, \quad \frac{dI}{dV} = -\frac{I}{V} \quad \text{at the MPP} \tag{4}$$

$$\frac{dP}{dV} > 0, \quad \frac{dI}{dV} > -\frac{I}{V} \quad \text{the left side of the MPP} \tag{5}$$

$$\frac{dP}{dV} < 0, \quad \frac{dI}{dV} < -\frac{I}{V} \quad \text{the right side of the MPP} \tag{6}$$

Therefore, the MPPT technique detects the location of the MPP by comparing the incremental conductance (dI/dV) with the instantaneous conductance (I/V). Once the MPP is calculated, the boost converter controller adjusts the output voltage from the PV module towards the reference voltage (V_{mpp}) by regulating the converter's duty cycle. In the conventional InCond MPPT method, the step-size of the duty cycle (D) is generally fixed. However, the larger step-size of the duty cycle increases the response of the MPPT technique but contributes excessive oscillations around the MPP instead of directly tracking it, thus producing a steady-state error and low efficiency. On the other hand, the smaller step-size decreases the oscillations around the MPP but slows down the dynamics of the MPPT technique. The solution to such a design dilemma is to use a variable step-size of the duty cycle that gets smaller towards the MPP. Fig.7 illustrates the flow chart of the proposed variable step-size InCond MPPT technique as compared to the conventional method. In the proposed MPPT technique, the step-size of the duty cycle is varied according to the location of the operating point of the PV module so that improves the tracking speed and accuracy of the MPPT controller. The variable step-size of the duty cycle can be obtained as follows [20], [21]:

$$D(k) = D(k-1) \pm N\left|\frac{P(k) - P(k-1)}{V(k) - V(k-1)}\right| \tag{7}$$

3) VSI CONTROLLER

The PV station is interfaced with the PCC busbar through 3-level, 3-phase Pulse Width Modulation (PWM) inverter. The control scheme of the VSI is described in Fig. 8. A Voltage-Oriented Control (VOC) system is used to maintain the DC-link voltage between the boost converter and the VSI at a constant value, and also control the injected reactive power from the PV station. The most important parts of the VSI controller are the Phase Locked Loop (PLL), the DC-link voltage controller, and the decoupled current controller. The PLL estimates the grid voltage angle (θ_{PLL}) that utilized for abc/d-q transformation and to synchronize the VSI output voltage with the PCC bus voltage [22]. As can be observed in Fig. 8, the first control loop is the DC-link
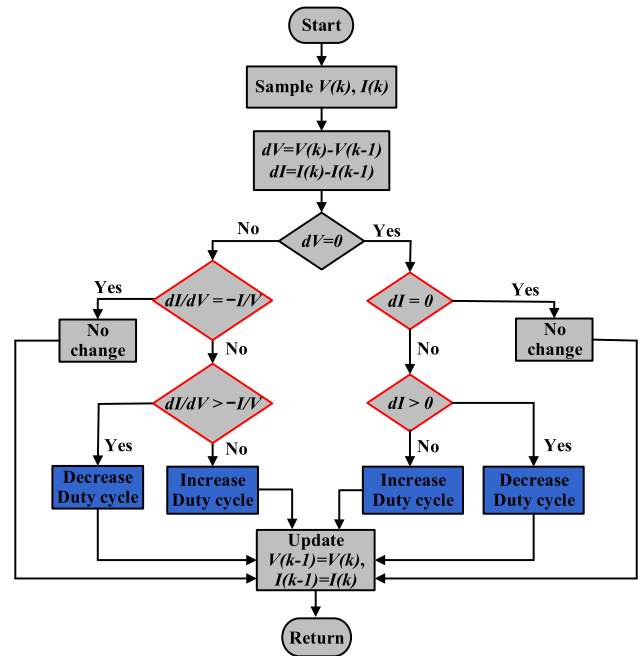
(a) Conventional InCond
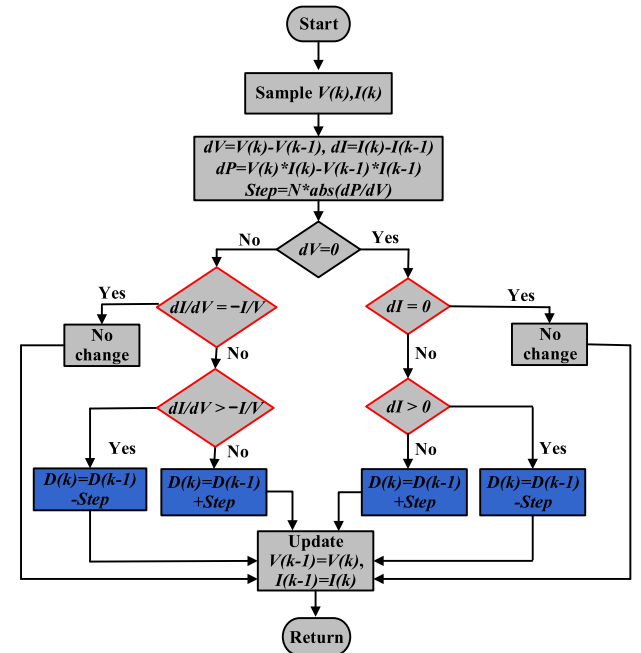
(b) Proposed variable step size

FIGURE 7. Flow chart for InCond MPPT algorithm.

voltage controller which applies to maintain the voltage of the DC-link capacitor at a specified constant value (500 V). This controller compares the measured DC-link voltage (V_{dc1}) with its reference value ($V_{dc1-ref}$) to estimate the reference d-axis component of the inverter current (I_{d-ref}).

The second control loop is the current controller which requires the inverter output current to be transformed and decoupled into active (I_d) and reactive (I_q) components,
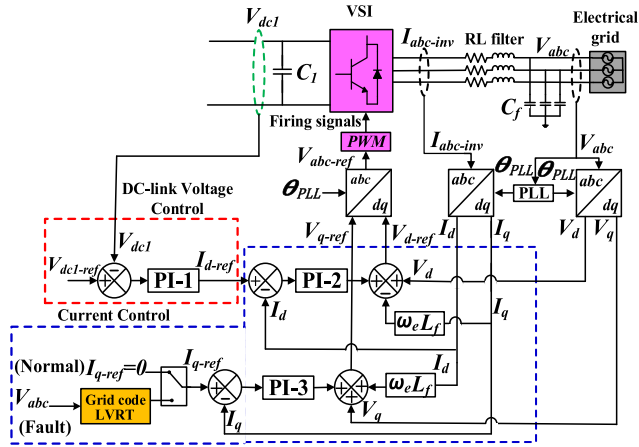
FIGURE 8. Control strategy of the VSI.

respectively. Generally, the active current component (I_d) is applied to regulate the DC-link voltage, while the reactive current component (I_q) is utilized to control the injected reactive power from the PV station. The current controller compares the (I_{d-ref}) from the DC-link voltage controller with the (I_d) to estimate the reference d-axis component of the inverter voltage (V_{d-ref}). Similarly, the reference q-axis current (I_{q-ref}) is set to zero to ensure unity power factor operation during the normal operation conditions and it is compared with the I_q to estimate reference voltage (V_{q-ref}). The setting parameters of the PI controllers applied in the VSI control strategy are provided in the Appendix. The characteristics of the DC-link voltage controller and the current controller can be determined as follows [23]:

$$I_{d\_ref} = K_{p\_1}\left(V_{dc1\_ref} - V_{dc1}\right) + K_{i\_1}\int \left(V_{dc1\_ref} - V_{dc1}\right) dt \tag{8}$$

$$V_{d\_ref} = V_d + \left(K_{p\_2}\left(I_{d\_ref} - I_d\right)\right. \\ \left. + K_{i\_2}\int \left(I_{d\_ref} - I_d\right) dt - \omega_e L_f I_q\right) \tag{9}$$

$$V_{q\_ref} = V_q + \left(K_{p\_3} + K_{i\_3}\int\right)\left(I_{q\_ref} - I_q\right) dt + \omega_e L_f I_d \tag{10}$$

The vector control technique is implemented to control of VSI. The vector control consists of two loops, namely first loop and second loop. The first loop is implemented to maintain a constant DC-link voltage while the second loop controls of the injected current. The current loop is designed to response faster to any disturbance comparing with the voltage loop. The open-loop transfer function of the current loop is given as [24]:

$$G_{i,ol}\left(s\right) = \left(K_{p-(2,3)} + \frac{K_{i-(2,3)}}{s}\right)\frac{1}{L_f s + R_f}\frac{1}{t_{pwm}s + 1} \tag{11}$$

Selecting the parameters of PI compensator of current controller is achieved using modulus optimum technique. The parameters of the compensator are selected to achieve unity gain for the closed-loop system. The parameters of current

loop's compensator are selected to be [24]:

$$K_{p(2,3)} = \frac{L_f}{t_{pwm}} \tag{12}$$

$$K_{i(2,3)} = \frac{R_f}{t_{pwm}} \tag{13}$$

The first DC-link loop is designed to maintain constant voltage at the VSI. The DC voltage can be stabilized by generating the required power from PV array. The reference signal and open-loop transfer function of the voltage controller are expressed as follows [24]:

$$G_{v,ol} = \left(K_{p-1} + \frac{K_{i-1}}{s}\right)\frac{1}{\tau_i s + 1}\frac{1}{C_f s} \tag{14}$$

where τ_i is the time constant for the inner current closed loop. Tuning the PI compensator is achieved using symmetrical optimum technique. The concept of the selected method is to increase the phase margin by operating the system at low frequency which leads to slow down the dynamic response. Since the first voltage loop should be slower than the second current loop, this technique is suitable to tune the parameters of PI compensator. The compensator parameters are calculated as follows [24]:

$$K_{p-1} = \frac{C_f}{K\sqrt{t_v \tau_i}} \tag{15}$$

$$K_{i-1} = \frac{K_{p-1}}{t_v} \tag{16}$$

where, the voltage gain (K) equals ($3V_d/V_{dc}$) and the time constant of voltage loop (t_v) equals ($\alpha^2 \tau_i$). The symmetrical factor (α) needs to be in a range between 2 to 4 [24].

B. WIND FARM CONFIGURATION
1) GAMESA G80- 2.0 mW WIND TURBINE
The implemented wind farm with a total rated power of 200 MW consists of 100 variable-speed DFIG-based wind turbines. Based on the literature survey that has been done in [5] about the most suitable wind turbines in different locations in Egypt, Gamesa G80-2.0 MW wind turbine is considered as the most feasible in Gabel El-Zeit region. The detailed specifications of Gamesa G80-2.0 MW wind turbine are listed in Table 2 [25]. The wind turbine model is implemented using the equations described in [26]–[28]. Also, Fig. 9 shows the power-speed curve of the wind turbine during the wind speed variation.

2) RSC CONTROL SYSTEM
The main task of the RSC controller is to track the maximum power of the wind turbine during the wind speed variation and control the injected reactive power from the DFIG stator into the grid. The Stator Flux-Oriented Control (SFOC) strategy is adopted to implement the decoupled control scheme of the RSC. This control technique requires the three-phase rotor current ($I_{r,abc}$) to be transformed and decoupled into the d-q axis components (I_{dr}, I_{qr}). Therefore, the stator active power (P_s) can be controlled through the I_{qr}, while the
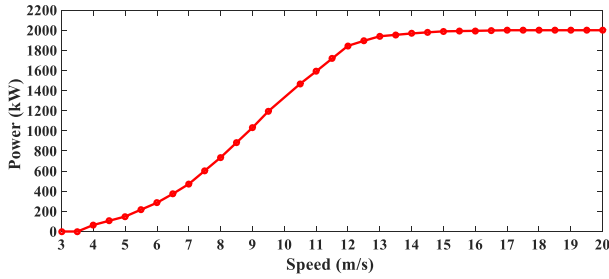
FIGURE 9. Power-speed curve of Gamesa G80-2.0 MW wind turbine.

FIGURE 10. Control system of the RSC.

stator reactive power (Q_s) can be regulated by the I_{dr} as follows [29]:

$$P_s = \frac{3}{2}\left[-V_{qs}i_{qs}\right] = \frac{3L_m}{2L_s}\left[\omega_e\Phi_{ds}i_{qr}\right] \quad (17)$$

$$Q_s = \frac{3\omega_e\Phi_{ds}}{2L_s}\left(\Phi_{ds} - L_m I_{dr}\right) \quad (18)$$

The control system of the RSC is described in Fig. 10. The vector technique is implanting based on its stability feature and rapid disturbance rejection. The q-axis component of the rotor current (I_{qr}) is used to track the peak power of the wind turbine during the change of wind speed. Thus, the I_{qr-ref} created from the rotor speed controller is compared with the I_{qr} to generate the V_{qr-ref}. On the other hand, the d-axis component of the rotor current (I_{dr}) is used to regulate the DFIG stator reactive power, where the reference value (Q_{ref}) is imposed to zero to maintain the wind farm at unity power factor. Then, the I_{dr-ref} generated from the reactive power controller is compared with the I_{dr} to estimate the V_{dr-ref}. The parameters of the RSC gains are listed in the Appendix. The RSC controller can be described as follows [30], [31]:

$$I_{dr\_ref} = K_{pr\_1}\left(Q_{ref} - Q_s\right) + K_{ir\_1}\int\left(Q_{ref} - Q_s\right)dt \quad (19)$$

$$V_{dr\_ref} = K_{pr\_2}\left(I_{dr\_ref} - I_{dr}\right) + K_{ir\_2}\int\left(I_{dr\_ref} - I_{dr}\right)dt \\ - (\omega_e - \omega_r)\sigma_s L_r I_{qr} \quad (20)$$

$$I_{qr\_ref} = K_{pr\_3}(\omega_{ref\_} - \omega_r) + K_{ir\_3}\int(\omega_{ref\_} - \omega_r)dt \quad (21)$$

$$V_{qr_{ref}} = K_{pr\_4}\left(I_{qr_{ref}} - I_{qr}\right) \\ + K_{ir\_4}\int\left(I_{qr\_ref} - I_{qr}\right)dt + (\omega_{e\_}\omega_r)(\frac{L_m^2}{L_s}i_{ms} \\ + \sigma_s L_r I_{dr}) \quad (22)$$

3) MPPT CONTROLLER: MODIFIED P&O MPPT TECHNIQUE

The MPPT technique is broadly used in the Wind Energy Conversion System (WECS) to extract the maximum power by searching the optimal operating point during the wind speed variation. In this work, a modified P&O MPPT strategy is implemented to capture the maximum power from the wind farm and enhance its overall efficiency during all the environmental conditions. This strategy has the advantages of being flexible, simple, more reliable, and easy for implementation since it does not require either prior knowledge of the wind

speed measurements or the wind turbine parameters [32]. The operating principle of this algorithm is based on perturbing the DFIG rotor speed (ω_r) in certain step-size and observing the resulting change in the wind turbine output power (P_m) to decide the subsequent perturbation direction until the MPP is achieved. If the generated power is increasing, the next perturbation is continued in the same direction (the sign of next perturbation is maintained), and it is reversed in the opposite direction otherwise. However, the conventional P&O MPPT technique has some demerits such as efficiency/rapidity trade-off and the divergence from the maximum power during the rapid variation of wind speed. Therefore, the large step-size of change in rotor speed enhances the rapidity of the controller to reach the MPP but contributes large oscillations around this point, and thus reducing the system efficiency. On the other hand, the small step-size improves the system efficiency but slows down its dynamic to reach the MPP, and therefore the algorithm may be incapable of extracting the peak power during the fast fluctuation of wind speed [33].

To overcome the aforementioned problem of the conventional P&O method, this paper proposes a modified P&O MPPT strategy based variable step-size to extract the maximum power from the wind farm. Fig. 11 demonstrates the operating principle and the flow chart of the proposed P&O MPPT technique. The idea behind this technique is to vary the direction and step-size of the perturbation in the rotor speed according to the distance between the operating point and the optimal MPP. Also, the step-size gets smaller when the output power is closer to the MPP to eliminate the oscillations around this point [34]. Therefore, this modified P&O MPPT algorithm creates a proper trade-off between the system efficiency and the tracking speed during the fast change of the wind speed.

4) GSC CONTROL SYSTEM

The GSC controller sustains the voltage of the DC-bus capacitor constant by keeping the balance between the active power flows from the RSC (P_{in}) and the injected active power from the GSC (P_{GSC}), as illustrated in (16)-(17) [8]. Also, it regulates the reactive power exchanged between the back-to-back converter and the electrical grid. Voltage-Oriented Control (VOC) system is utilized to achieve the decoupled control scheme of the GSC.
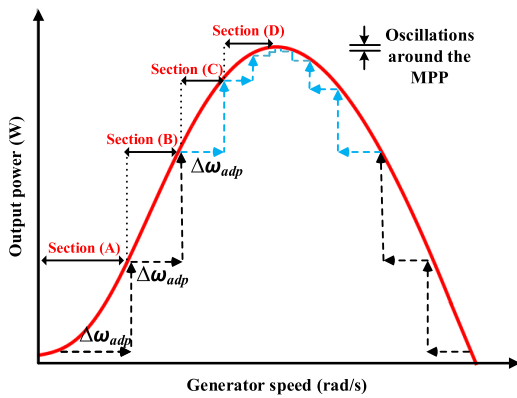
(a) Operating principle of P&O
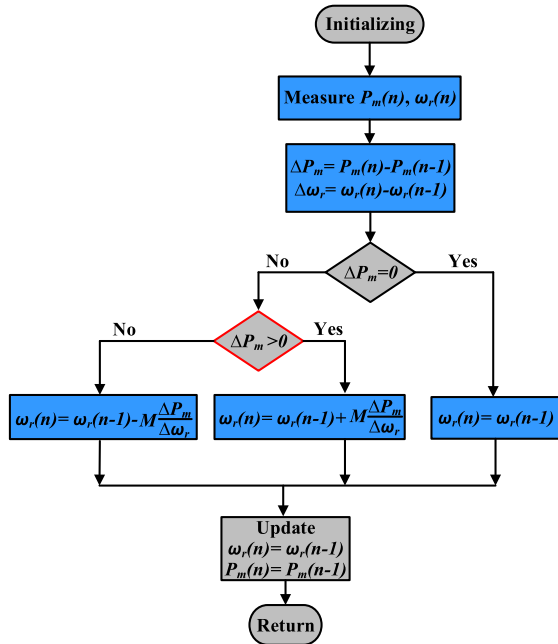
(b) Flow chart of the proposed P&O

FIGURE 11. Proposed variable step-size P&O MPPT technique.

Therefore, the injected active power from GSC (P_{GSC}) and the DC-bus capacitor voltage (V_{dc2}) is controlled by the Idg, while the transferred reactive power from GSC (Q_{GSC}) is adjusted through the Iqg as follows [35], [36]:

$$W = \int P_{dc}\, dt = \frac{1}{2} C_2 V_{dc2} \qquad (23)$$

$$\frac{dV_{dc2}}{dt} = \frac{P_{dc}}{C_2 V_{dc2}}, \quad P_{dc} = P_{in} - P_{GSC} \qquad (24)$$

$$C_2 \frac{dV_{dc2}}{dt} = \frac{3m}{4\sqrt{2}} I_{dg} - I_{or} \qquad (25)$$

$$Q_{GSC} = \frac{3}{2}\left(V_q I_{dg} - V_d I_{qg}\right) = -\frac{3}{2} V_d I_{qg} \qquad (26)$$

The control system of the GSC is illustrated in Fig. 12. The d-axis component of the GSC current (I_{dg}) is used to maintain the voltage of the DC-bus capacitor at its reference value (1150 V). Thus, the I_{dg-ref} generated from the DC-link
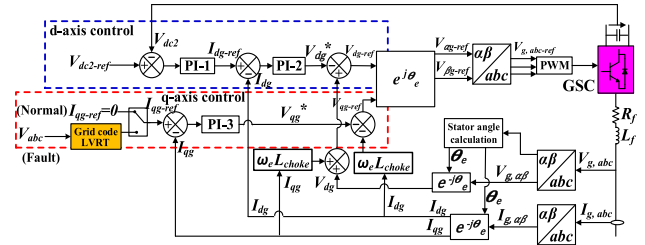
FIGURE 12. Control system of the GSC.

voltage controller is compared with the I_{dg} to generate the (V_{dg-ref}). On the other hand, the q-axis component of the GSC current (I_{qg}) is utilized to control the reactive power transferred to the grid through the back-to-back converter. During the normal operation conditions, the (I_{qg-ref}) is set to zero to ensure unity power factor operation. The setting parameters of the PI controllers used in the GSC control system are provided in the Appendix. Then, the I_{qg} is compared with the reference I_{qg-ref} to estimate the V_{qg-ref}. The GSC controller can be expressed as follows [35]:

$$I_{dg\_ref} = K_{pg\_1}\left(V_{dc2\_ref} - V_{dc2}\right) + K_{ig\_1} \int \left(V_{dc2\_ref} - V_{dc2}\right) dt \qquad (27)$$

$$V_{dg_{ref}} = K_{pg\_2}\left(I_{dg\_ref} - I_{dg}\right) + K_{ig\_2} \int \left(I_{dg\_ref} - I_{dg}\right) dt + V_d + \omega_e L_{choke} I_{qg} \qquad (28)$$

$$V_{qg_{ref}} = K_{pg\_3}\left(I_{qg\_ref} - I_{qg}\right) + K_{ig\_3} \int \left(I_{qg\_ref} - I_{qg}\right) dt - \omega_e L_{choke} I_{dg} \qquad (29)$$

## IV. SIMULATION RESULTS AND DISCUSSION

The proposed hybrid power system as shown in Fig. 5 is implemented and simulated using MATLAB/SIMULINK environment to validate the effectiveness of the proposed MPPT techniques and the robustness of the control strategies during the external disturbances. Moreover, actual variations of the solar irradiance and the wind speed in Gabel El-Zeit region are analyzed as a case study of realistic changes in the climatic conditions. This section is divided into three parts 1) performance of the PV station under the solar irradiation variation 2) performance of the wind farm during the change of the wind speed 3) hybrid power system performance at the PCC busbar.

A. PV STATION PERFORMANCE

In this subsection, the dynamic performance of the PV station during the real variation of the irradiance in the study region is discussed to evaluate the efficiency of the proposed InCond MPPT technique and the VSI control strategy. Fig. 13 (a) shows the monthly average solar irradiance in Gabel El-Zeit region [13]. The solar radiation varies from 182.8 W/m² in winter months to 359.7 W/m² in summer months. Fig. 13 (b) depicts the output voltage
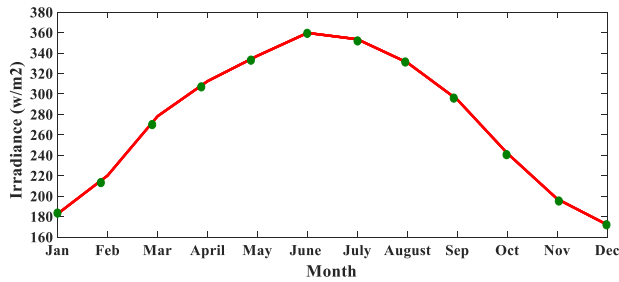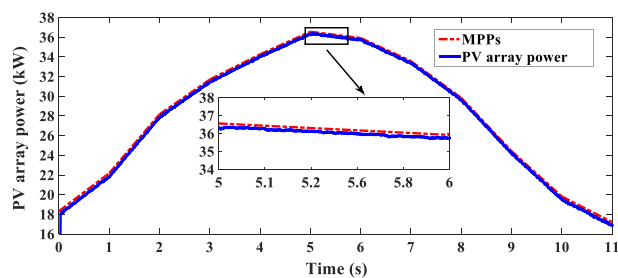
(a) Solar irradiance in the site under study
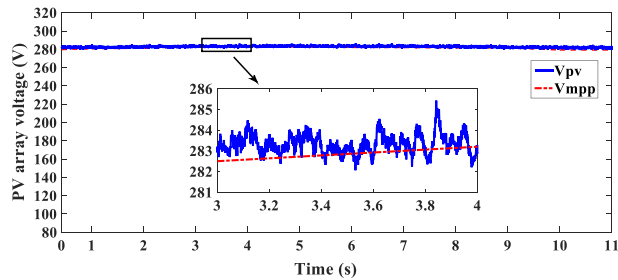
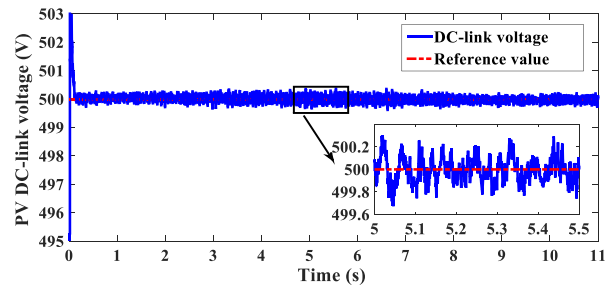(b) PV array voltage
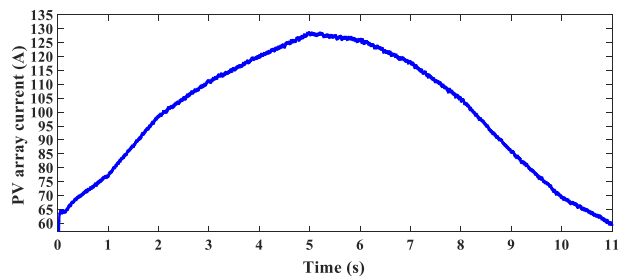
(c) PV array current

(d) PV array power and MPPs

FIGURE 13. PV array side results.

of the PV array. It can be noticed that the proposed MPPT controller converges correctly the operating voltage of the PV array towards the V_{mpp} that corresponds to each irradiance level. Fig. 13 (c) shows that the PV array current follows the same scenario of the solar irradiance variation. The current increases significantly from 63.95 A to 128.6 A, in response to the change of the irradiance from 182.8 W/m^2 in January to 359.7 W/m^2 in June. Then, the PV array current drops sharply to 59.6 A as the irradiation decreases considerably to 172 W/m^2 in December. As shown in Fig. 13 (d), the MPPT control strategy tracks accurately the MPPs. Therefore, the output power of PV rises from 18.1 kW in January to its

maximum value (36.35 kW) in June, then it decreases to its minimum value (16.9 kW) in December.

Consequently, the effectiveness of the VSI control system is validated. Fig. 14 (a) illustrates that the DC-link voltage controller adjusts successfully the voltage of the DC-link capacitor at its reference value (500 V) regardless of the solar irradiance variation. Fig. 14 (b) depicts the action of the current controller. It can be seen that the active current component (I_d) varies with the level of solar irradiance, while the reactive power component (I_q) coincides with its reference at zero value to maintain the VSI at the unity power factor. Fig. 14 (c) ensures the synchronization of the VSI current (I_a) with the voltage (V_a).


(a) PV DC-link voltage (V_{dc1}).
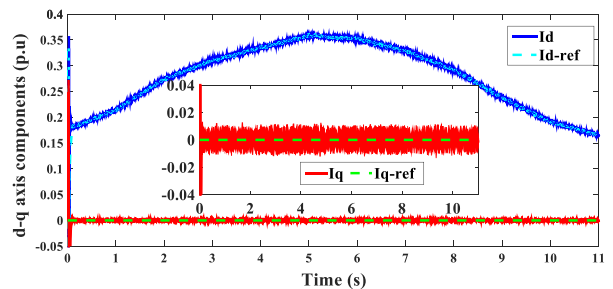
(b) d-q axis components of the current controller
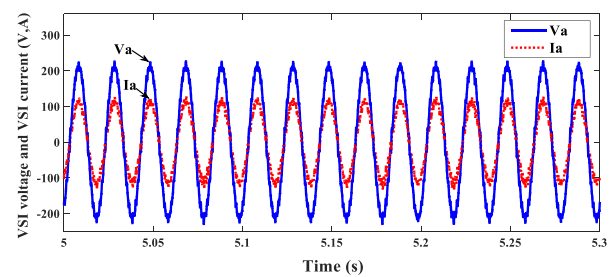
(c) PV array current

**FIGURE 14.** Dynamic action of the VSI controller.

Fig. 15 illustrates the dynamic performance of the PV station at the B1-bus. Fig. 15 (a) shows that the injected 3-phase current from the PV station follows the variation of the generated active power since the voltage remains constant and synchronized with the grid voltage, as depicted in Fig. 15 (b). Also, Fig. 15 (c) demonstrates the injected active power and reactive power from the whole PV station.
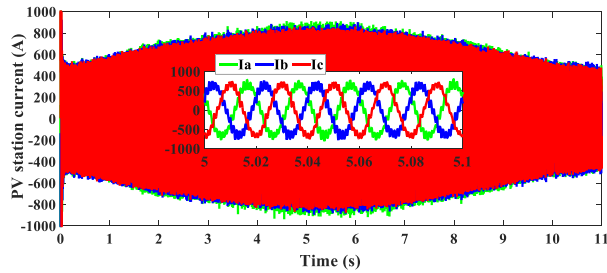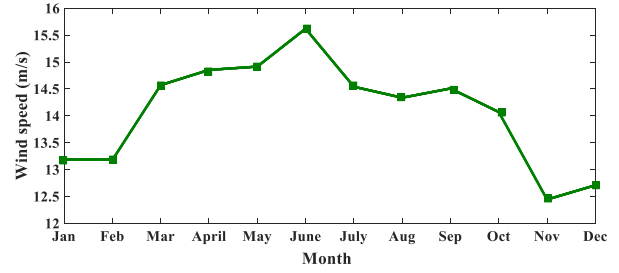
(a) PV station current
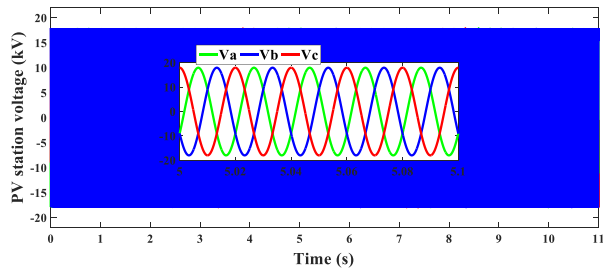
(b) PV station voltage
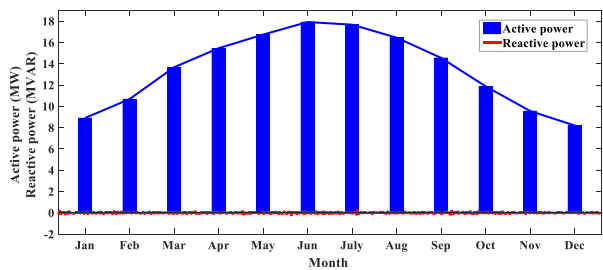
(c) Injected active and reactive power from the PV station

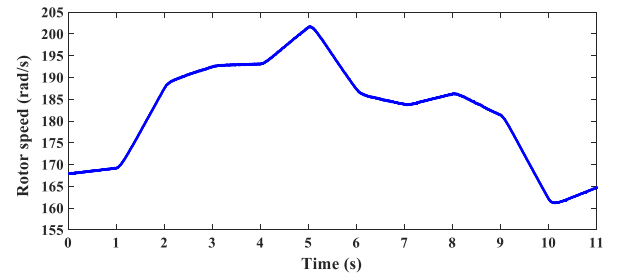**FIGURE 15.** Dynamic performance of the PV station at the B1-bus.

(a) Wind speed in the site under study

(b) Rotor speed

(c) Turbine and DFIG torque

(d) Tip speed ratio (λ)

(e) Performance coefficient (C_P)

FIGURE 16. Gamesa wind turbine results.

It can be observed that the injected active power changes according to the level of solar irradiance. Therefore, the active power increases significantly from 8.9 MW in January to its maximum value (17.9 MW) in June, then it falls drastically to the minimum value of 8.2 MW in December. On the other hand, the delivered reactive power is kept at zero to sustain the PV station at the unity power factor.
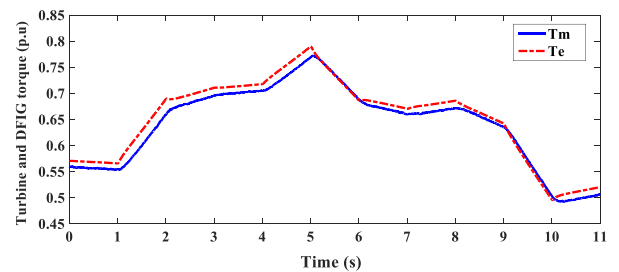
B. WIND FARM PERFORMANCE

This subsection investigates the dynamic behavior of the wind farm under the actual change of the wind speed in Gabel El-Zeit region. The performance is analyzed to evaluate the action of the RSC and GSC controllers and validate the effectiveness of the proposed P&O MPPT strategy. Fig. 16 (a) shows the monthly average wind speed at 60 m hub height in the study area. The wind speed ranges between 12.44 m/s in November and 15.62 m/s in June with an annual average value of 14.08 m/s. Fig. 16 (b) shows the tracking response of the rotor speed to extract the maximum power during the wind speed variation. The rotor speed rises from 167.9 rad/s to 201.5 rad/s, in response to the increase in the
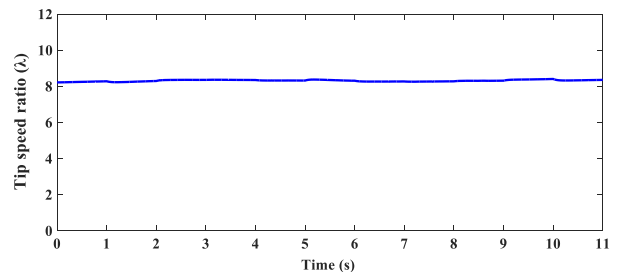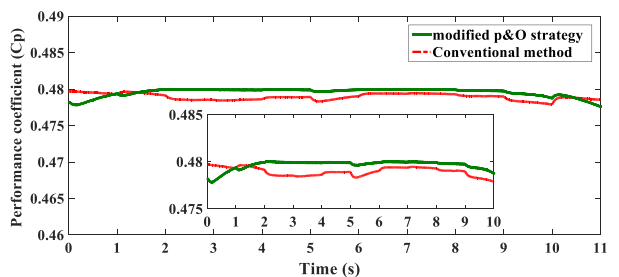
wind speed from 13.18 m/s in January to 15.62 m/s in June. Then, it decreases gradually until reaching the minimum

value of 164.7 rad/s in November that corresponds to the lowest wind speed (12.44 m/s). Also, Fig. 16 (c) demonstrates that the DFIG torque converges accurately towards the MPP of the wind turbine torque. The wind turbine characteristics such as the tip speed ratio (λ) and the performance coefficient (C_p) are presented in Fig. 16 (d, e), respectively. It can be noted that the tip speed maintains at its optimal value (8.1) irrespective of the wind speed variation. Besides, as compared to the conventional MPPT method, the proposed P&O MPPT technique successfully sustains the optimal value of the performance coefficient, $C_p = 0.48$ [37], which illustrates that the rotor speed is well controlled to capture the maximum power. The performance coefficient is an excellent indication of the wind turbine efficiency.

The effectiveness of the GSC and RSC controllers is validated. Fig. 17 (a) illustrates that the GSC controller has successfully stabilized the DC-bus voltage (V_{dc2}) to the desired value (1150 V) regardless of the wind speed change. Moreover, Fig. 17 (b) ensures the credibility of the RSC and GSC controllers in keeping the DFIG operation at the unity power factor since the injected current (I_a) is in the same phase with the DFIG voltage (V_a). The following figures demonstrate the dynamic performance of the wind farm at the B2-bus. Fig. 17 (c) shows that the injected 3-phase current from the wind farm follows the change of the generated active power since the voltage maintains constant and it is synchronized with the grid voltage, as depicted in Fig. 17 (d). Also, Fig. 17 (e) shows the injected active power and reactive power from the wind farm. It can be seen that the generated active power varies according to the level of wind speed. Therefore, during the first half of the year, the active power increases dramatically from 127.6 MW in January to the rated value (200 MW) in June, then it decreases gradually until reaching the minimum value of 112.4 MW in November. On the other hand, the injected reactive power is kept at zero to maintain the wind farm at the unity power factor.

## C. HYBRID POWER SYSTEM PERFORMANCE AT THE PCC BUS

In this subsection, the dynamic performance of the hybrid power system at the PCC bus is discussed. Fig. 18 (a) illustrates the injected active power into the electrical network from each generation source when the other source is disconnected. It can be seen that both the PV station or the wind farm will continue to provide its maximum output power even though the other power source is failed. Fig. 18 (b) shows the monthly electricity production from the PV station and the wind farm in the hybrid renewable energy system. It can be noted that the total annual electricity generation from the hybrid power system is 1509.85 GWh/year. From this total annual electricity production, 118.15 GWh/year (7.83 %) generates from the PV station and 1391.7 GWh/year (92.17%) comes from the wind farm. Also, the maximum electricity generation can be obtained in June with 165.1 GWh (152.2 GWh from the wind farm and 12.9 GWh
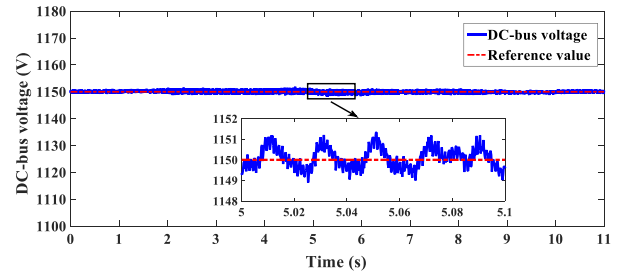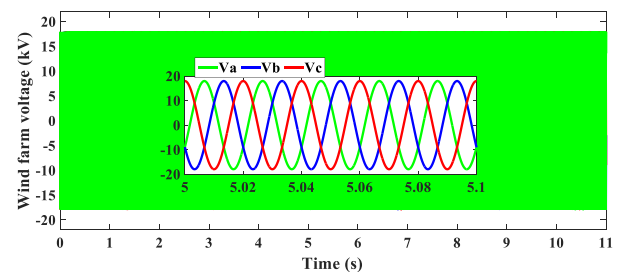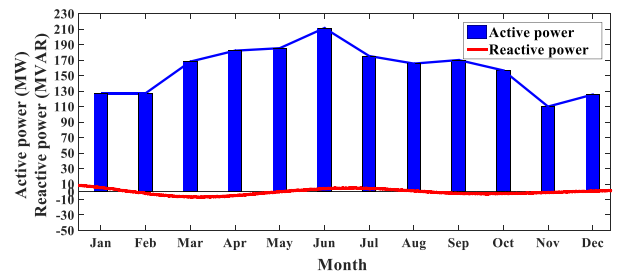

(a) DC-bus voltage (V_{dc2}).
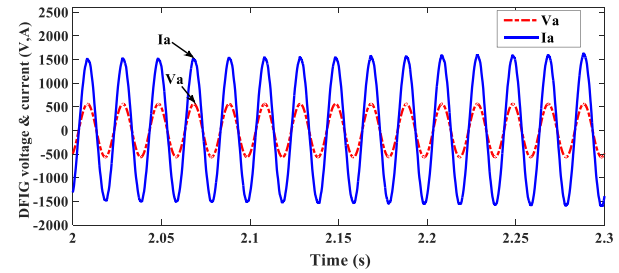
(b) DFIG voltage and DFIG current
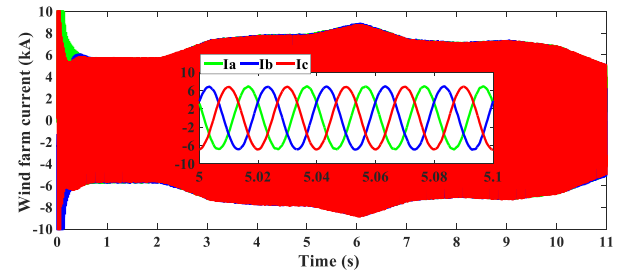
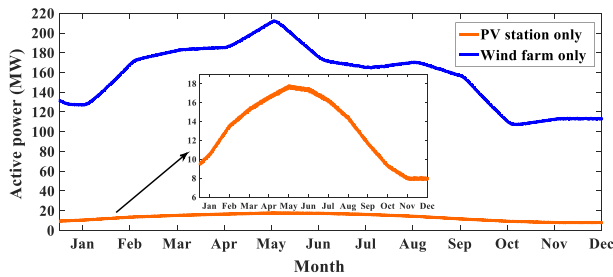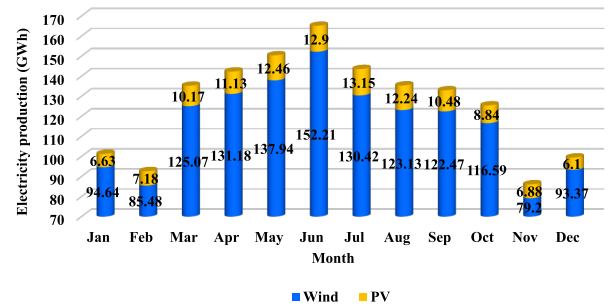

(c) Wind farm current

(d) Wind farm voltage

(e) Injected active and reactive power from the wind farm

FIGURE 17. Dynamic performance of the wind speed at the B2-bus.
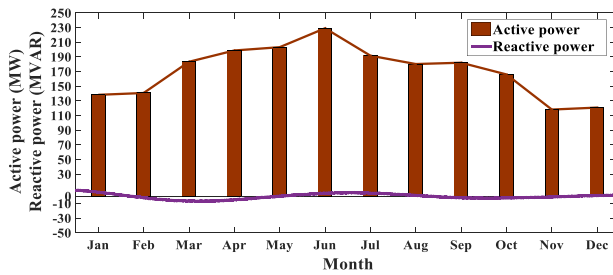
from PV station), while the lowest electrical energy generation occurs in November with 86.1 GWh.
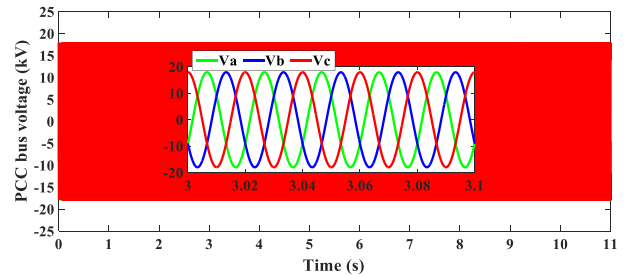
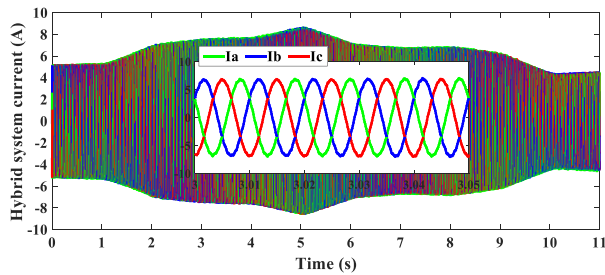(a) Injected active power from each generation source

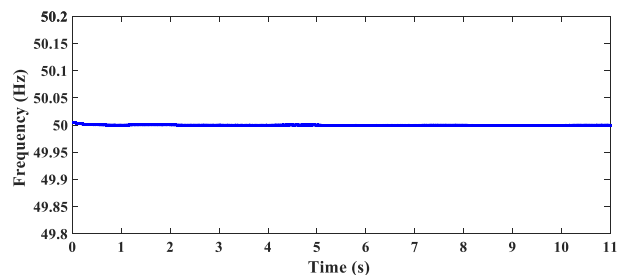(b) Monthly electricity from the PV station and the wind farm

(c) Generated active and reactive power from the hybrid system

(d) PCC bus voltage

(e) Injected current from the hybrid power system

(f) Frequency

FIGURE 18. Performance of the hybrid system at the PCC bus.

Fig. 18 (c) shows the injected active power and reactive power from the hybrid power system into the electrical grid. It can be noticed that the generated active power increases significantly from 136.5 MW in January to the maximum value (217.9 MW) in June, then it decreases gradually till reaching the lowest value (120.6 MW) in November. Moreover, the used control strategies keep successfully the injected reactive power at zero to sustain the hybrid power system operation at the unity power factor. Fig. 18 (d) demonstrates that the used control strategies sustain always the PCC bus voltage constant regardless of the magnitude of the generated active power and the variations of climatic conditions. Fig. 18 (e) depicts the injected current from the hybrid power system into the electrical grid. The change of current amplitude reflects the variation of injected active power as the hybrid system voltage remains constant. Fig. 18 (f) illustrates the frequency of the generated power which coincides with the Egyptian grid frequency (50 Hz).

V. CONCLUSION
This paper presented the detailed design, control strategy, and performance analysis of 250 MW grid-connected PV/wind hybrid power system in Gabel El-Zeit region, Egypt. This area is characterized by a good level of solar irradiation with an annual average value of 199.75 kWh/m^2 and powerful wind speed with an average value of 14.08 m/s at 60 m hub height. The proposed hybrid power system consists of 50 MW PV station based Sanyo HIP-200B PV module and 200 MW wind farm based Gamesa G80 wind turbine and it is integrated with the grid through the main PCC bus to support the system performance. The hybrid power system is adjusted to work at the unity power factor and also the MPPT algorithms are applied to capture the optimum power from the hybrid system under the changes of climatic conditions. Adaptive InCond MPPT technique based variable step-size is applied to the boost converter to extract the maximum power from the PV station during the solar irradiance variation. On the other

hand, a modified P&O MPPT strategy is implemented on the RSC of DFIG to obtain the maximum power from the wind farm during the change of wind speed.

Moreover, this paper analyzed the actual monthly changes of solar irradiance and wind speed in the study area to evaluate the dynamic performance of the hybrid system and validate the efficiency of the proposed MPPT techniques and the control systems. The simulation results have illustrated that the proposed InCond MPPT algorithm tracks accurately the MPPs, where the PV station power increases significantly from 8.9 MW in January to its maximum value (17.9 MW) in June, then it falls drastically to the minimum value of 8.2 MW in December. Also, the DC-link voltage controller of the VSI adjusts successfully the DC-link voltage at its reference value (500 V) regardless of the solar irradiance variation.

Furthermore, the proposed P&O MPPT strategy sustains the optimal value of the wind turbine performance coefficient, $C_p = 0.48$, to extract the maximum power from the wind farm during the change of wind speed. Therefore, the active power rises dramatically from 127.6 MW in January to the rated value (200 MW) in June, then it decreases gradually until reaching the minimum value of 112.4 MW in November. Besides, the GSC controller has successfully stabilized the DC-bus voltage to the desired value (1150 V) regardless of the wind speed change.

Additionally, the simulation results have shown that the total annual electricity generation from the hybrid power system is 1509.85 GWh/year, where 118.15 GWh/year (7.83 %) generates from the PV station and 1391.7 GWh/year (92.17%) comes from the wind farm. Moreover, the control system always maintains the hybrid power system at the unity power factor as the injected reactive power is kept at zero. Also, the PCC bus voltage is sustained perfectly constant irrespective of the changes in climatic conditions and the magnitude of generated active power.

APPENDIX
See Table 4.

TABLE 4. PI controllers' parameters.

The VSI gains	DC-link voltage control	K_{p-1}	7
		K_{i-1}	800
	Current control	K_{p-2}	0.3
		K_{i-2}	20
		K_{p-3}	0.3
		K_{i-3}	20
The RSC gains	d-axis current control	K_{pr-1}	1
		K_{ir-1}	0.05
		K_{pr-2}	0.6
		K_{ir-2}	8
	Speed controller	K_{pr-3}	1
		K_{ir-3}	0.2
	q-axis current control	K_{pr-4}	0.6
		K_{ir-4}	8
The GSC gains	d-axis current control	K_{pg-1}	8
		K_{ig-1}	400
		K_{pg-2}	0.83
		K_{ig-2}	5
	q-axis current control	K_{pg-3}	0.83
		K_{ig-3}	5

REFERENCES

[1] K. D. Patlitzianas, "Solar energy in Egypt: Significant business opportunities," *Renew. Energy*, vol. 36, no. 9, pp. 2305–2311, Sep. 2011.

[2] H. M. Sultan, O. N. Kuznetsov, and A. A. Z. Diab, "Site selection of large-scale grid-connected solar PV system in egypt," in *Proc. IEEE Conf. Russian Young Researchers Electr. Electron. Eng. (EIConRus)*, Jan. 2018, pp. 813–818.

[3] Ministry of Electricity and Renewable Energy. (2018). *New and Renewable Energy Authority (NREA) Annual Report for the Egypt*. [Online]. Available: http://www.nrea.gov.eg/Content/reports/Englishv2AnnualReport.pdf

[4] M. EL-Shimy, "Viability analysis of PV power plants in Egypt," *Renew. Energy*, vol. 34, no. 10, pp. 2187–2196, Oct. 2009.

[5] M. G. M. A. Y. Hatata and M. Rana Elmahdy, "Analysis of wind data and assessing wind energy potentiality for selected locations in Egypt," *Int. J. Sci. Eng. Res.*, vol. 6, p. 6, Mar. 2015.

[6] O. Noureldeen, I. Hamdan, and B. Hassanin, "Design of advanced artificial intelligence protection technique based on low voltage ride-through grid code for large-scale wind farm generators: A case study in egypt," *Social Netw. Appl. Sci.*, vol. 1, no. 6, p. 515, Jun. 2019.

[7] O. Noureldeen and A. Rashad, "Modeling and investigation of gulf el-zayt wind farm for stability studying during extreme gust wind occurrence," *Ain Shams Eng. J.*, vol. 5, no. 1, pp. 137–148, Mar. 2014.

[8] O. Noureldeen, M. M. M. Youssef, and B. Hassanin, "Stability improvement of 200 MW gabal el-zayt wind farm connected to electrical grid using supercapacitor and static synchronous compensator during extreme gust," *Social Netw. Appl. Sci.*, vol. 1, no. 4, p. 331, Apr. 2019.

[9] F. Diab, H. Lan, L. Zhang, and S. Ali, "An environmentally friendly factory in Egypt based on hybrid photovoltaic/wind/diesel/battery system," *J. Cleaner Prod.*, vol. 112, pp. 3884–3894, Jan. 2016.

[10] A. Fathy, "A reliable methodology based on mine blast optimization algorithm for optimal sizing of hybrid PV-wind-FC system for remote area in Egypt," *Renew. Energy*, vol. 95, pp. 367–380, Sep. 2016.

[11] E. Aboud, A. Salem, and K. Ushijima, "Subsurface structural mapping of Gebel El-Zeit area, Gulf of Suez, Egypt using aeromagnetic data," *Earth, Planets Space*, vol. 57, pp. 755–760, 2005.

[12] [Online]. Available: https://www.google.com/maps

[13] Ministry of Electricity and Renewable Energy. (2018). *New and Renewable Energy Authority (NREA) The Solar Atlas of Egypt*. Available:. [Online]. Available: http://www.nrea.gov.eg/Content/files/SOLAR ATLAS 2018 digital1.pdf

[14] *Sanyo*. [Online]. Available: www.sanyo.co.jp/clean/solar/hit_e/download.html

[15] L. Zhu, Q. Li, M. Chen, K. Cao, and Y. Sun, "A simplified mathematical model for power output predicting of building integrated photovoltaic under partial shading conditions," *Energy Convers. Manage.*, vol. 180, pp. 831–843, Jan. 2019.

[16] M. Killi and S. Samanta, "Modified perturb and observe MPPT algorithm for drift avoidance in photovoltaic systems," *IEEE Trans. Ind. Electron.*, vol. 62, no. 9, pp. 5549–5559, Sep. 2015.

[17] S. Bae and A. Kwasinski, "Dynamic modeling and operation strategy for a microgrid with wind and photovoltaic resources," *IEEE Trans. Smart Grid*, vol. 3, no. 4, pp. 1867–1876, Dec. 2012.

[18] K. S. Tey and S. Mekhilef, "Modified incremental conductance MPPT algorithm to mitigate inaccurate responses under fast-changing solar irradiation level," *Sol. Energy*, vol. 101, pp. 333–342, Mar. 2014.

[19] L. Zhang, S. S. Yu, T. K. Chau, T. Fernando, and H. H.-C. Iu, "An advanced incremental conductance MPPT technique considering time-varying solar irradiances," *IOP Conf. Ser., Earth Environ. Sci.*, vol. 322, Sep. 2019, Art. no. 012017.

[20] F. Liu, S. Duan, F. Liu, B. Liu, and Y. Kang, "A variable step-size INC MPPT method for PV systems," *IEEE Trans. Ind. Electron.*, vol. 55, no. 10, pp. 2622–2628, Oct. 2008.

[21] Y. WeiFeng and C. Yan, "Maximum power point tracking of PV systems based on a novel adaptive variable step size INC MPPT method," *J. Phys., Conf. Ser.*, vol. 1213, Jun. 2019, Art. no. 042001.

[22] A. Althobaiti, M. Armstrong, and M. A. Elgendy, "Current control of three-phase grid-connected PV inverters using adaptive PR controller," in *Proc. 7th Int. Renew. Energy Congr. (IREC)*, Mar. 2016, pp. 1–6.

[23] A. S. Al-Ogaili, I. B. Aris, R. Verayiah, A. Ramasamy, M. Marsadek, N. A. Rahmat, Y. Hoon, A. Aljanad, and A. N. Al-Masri, "A three-level universal electric vehicle charger based on voltage-oriented control and pulse-width modulation," *Energies*, vol. 12, no. 12, p. 2375, Jun. 2019.

[24] A. Tazay and Z. Miao, "Control of a three-phase hybrid converter for a PV charging station," *IEEE Trans. Energy Convers.*, vol. 33, no. 3, pp. 1002–1014, Sep. 2018.

[25] Gamesa. (2010). *Gamesa G80-2.0 MW*. Accessed: Sep. 7, 2010. [Online]. Available: http://www.gamesa corp.com/files/File/G80-ingles.pdf

[26] A. Baghbany Oskouei, M. R. Banaei, and M. Sabahi, "Hybrid PV/wind system with quinary asymmetric inverter without increasing DC-link number," *Ain Shams Eng. J.*, vol. 7, no. 2, pp. 579–592, Jun. 2016.

[27] M. Izadbakhsh, A. Rezvani, and M. Gandomkar, "Dynamic response improvement of hybrid system by implementing ANN-GA for fast variation of photovoltaic irradiation and FLC for wind turbine," *Arch. Electr. Eng.*, vol. 64, no. 2, pp. 291–314, Jun. 2015.

[28] E. M. Natsheh, A. Albarbar, and J. Yazdani, "Modeling and control for smart grid integration of solar/wind energy conversion system," in *Proc. 2nd IEEE PES Int. Conf. Exhib. Innov. Smart Grid Technol.*, Dec. 2011, pp. 1–8.

[29] A. Parida and D. Chatterjee, "Cogeneration topology for wind energy conversion system using doubly-fed induction generator," *IET Power Electron.*, vol. 9, no. 7, pp. 1406–1415, Jun. 2016.

[30] A. Parida and D. Chatterjee, "An improved control scheme for grid connected doubly fed induction generator considering wind-solar hybrid system," *Int. J. Electr. Power Energy Syst.*, vol. 77, pp. 112–122, 2016.

[31] M. Chen, D. Fan, H. Fang, Y. Zhu, and P. Chen, "Control strategy of excitation converter in doubly-fed induction generator wind power generation system," in *Proc. IEEE Conf. Energy Internet Energy Syst. Integr.*, Nov. 2017, pp. 1–5.

[32] S. M. Tripathi, A. N. Tiwari, and D. Singh, "Grid-integrated permanent magnet synchronous generator based wind energy conversion systems: A technology review," *Renew. Sustain. Energy Rev.*, vol. 51, pp. 1288–1305, Nov. 2015.

[33] Y. Daili, J.-P. Gaubert, and L. Rahmani, "Implementation of a new maximum power point tracking control strategy for small wind energy conversion systems without mechanical sensors," *Energy Convers. Manage.*, vol. 97, pp. 298–306, Jun. 2015.

[34] D. Kumar and K. Chatterjee, "A review of conventional and advanced MPPT algorithms for wind energy systems," *Renew. Sustain. Energy Rev.*, vol. 55, pp. 957–970, Mar. 2016.

[35] T. R. Ayodele, A.-G. A. Jimoh, J. Munda, and J. Agee, "Dynamic response of a wind farm consisting of doubly-fed induction generators to network disturbance," in *Simulation and Modeling Methodologies, Technologies and Applications*. Springer, 2013, pp. 131–150.

[36] J. Mohammadi, S. Vaez-Zadeh, E. Ebrahimzadeh, and F. Blaabjerg, "Combined control method for grid-side converter of doubly fed induction generator-based wind energy conversion systems," *IET Renew. Power Gener.*, vol. 12, no. 8, pp. 943–952, Jun. 2018.

[37] R. M. Linus and P. Damodharan, "Maximum power point tracking method using a modified perturb and observe algorithm for grid connected wind energy conversion systems," *IET Renew. Power Gener.*, vol. 9, no. 6, pp. 682–689, Aug. 2015.

AHMED MOHAMMED AHMED IBRAHIM was born in Qena, Egypt, in September 1992. He received the B.Sc. degree in electrical engineering and the M.Sc. degree from South Valley University, in 2014 and 2018, respectively. He worked as an Automation Engineer for two years. He is currently working as a Teaching Assistant with the Faculty of Engineering, South Valley University. His researches of interest include the integration of renewable energy sources, PV/wind hybrid power systems, and control of the smart grid and micro-grid systems.

OMAR NOURELDEEN received the Ph.D. degree in electrical power and machines from the Faculty of Engineering, Cairo University, in 2004. He is currently a Professor with the Department of Electrical Engineering, Faculty of Engineering, South Valley University, Egypt. From 2004 to 2006, he has been an Assistant Professor with the Department of Electrical Engineering, Faculty of Energy Engineering, Aswan University. From 2007 to 2013, he was an Assistant Professor with the Department of Electrical Engineering, Faculty of Engineering, South Valley University, where he was an Associate Professor, from 2014 to 2019. His fields of interest are digital protection of power systems, power system stability, and renewable energy systems.

AHMAD F. TAZAY was born in Jeddah, Saudi Arabia, in January 1985. He received the B.Sc. degree in electrical engineering from Umm Al-Qura University, in 2007, and the M.Sc. and Ph.D. degrees from the University of South Florida, USA, in 2013 and 2018, respectively. He is currently working as an Assistant Professor and the Chair of the Department of Electrical Engineering, Al Baha University, Saudi Arabia. His researches of interest include integration of renewable energy, designing of power electronics, and control of smart grid and micro-grid.

I. HAMDAN was born in Qena, Egypt, in 1985. He received the B.Sc. and M.Sc. degrees in industrial electronics and control engineering from the Faculty of Electronic Engineering, Menoufia University, Egypt, in 2008 and 2015, respectively, and the Ph.D. degree from the Department of Electrical Engineering, Faculty of Engineering, South Valley University, Egypt, in 2019. He is currently an Assistant professor with the Department of Electrical Engineering, Faculty of Engineering, South Valley University. His current research interests include control engineering, artificial intelligence, large-scale systems, and renewable energy systems.

● ● ●